

Supplemental Materials for: Possible many-body localization in a long-lived finite-temperature ultracold quasi-neutral molecular plasma

John Sous^{1,2} and Edward Grant^{1,3,*}

¹*Department of Physics & Astronomy, University of British Columbia, Vancouver, BC V6T 1Z3, Canada*

²*Stewart Blusson Quantum Matter Institute, University of British Columbia,
Vancouver, British Columbia, V6T 1Z4, Canada*

³*Department of Chemistry, University of British Columbia, Vancouver, BC V6T 1Z3, Canada*

I. DOUBLE-RESONANT PRODUCTION OF A STATE SELECTED MOLECULAR RYDBERG GAS

Laser pulses, ω_1 and ω_2 , cross a molecular beam to define a Gaussian ellipsoidal volume in which a sequence of resonant electronic transitions transfer population from the X $^2\Pi_{1/2}$ ground state of nitric oxide to an intermediate state, A $^2\Sigma^+$ with angular momentum neglecting spin, $N' = 0$, and then to a specified level in the mixed $n_0 f(2)$ Rydberg series to create a state-selected Rydberg gas of nitric oxide, in which quantities (0) and (2) refer to rotational quantum numbers of the NO $^+$ $^1\Sigma^+$ cation core.

The intensity of ω_1 determines the density of Rydberg molecules formed by saturated absorption of ω_2 . For a given ω_1 intensity, the peak Rydberg gas density varies with $\omega_1 - \omega_2$ delay according to the well-known decay rate of the A $^2\Sigma^+$ state. Choosing I_{ω_1} and $\Delta t_{\omega_1 - \omega_2}$, we precisely control the initial peak density of the Rydberg gas ellipsoid over a two-decade range from $\rho_0 = 10^{10}$ to 10^{12} cm^{-3} [S1].

In the core of this ellipsoid, Rydberg molecules, propagating in the molecular beam have a local longitudinal temperature of $T_{||} = 500 \text{ mK}$ and a transverse temperature, $T_{\perp} < 5 \text{ mK}$. These molecules interact at a density-determined rate to form NO $^+$ ions and free electrons. Initially created electrons collide with Rydberg molecules to trigger electron-impact avalanche on a time-scale that varies with density from nanoseconds to microseconds (see below).

II. SELECTIVE FIELD IONIZATION SPECTROSCOPY OF ELECTRON BINDING ENERGY

Selective field ionization (SFI) produces an electron signal waveform that varies with the amplitude of a linearly rising electrostatic field. Electrons in a Rydberg state with principal quantum number, n , ionize diabatically when the field amplitude reaches the electron binding energy threshold, $1/9n^2$ [S2].

For low density Rydberg gases, SFI has served as an exacting probe of the coupling of electron orbital angular momentum coupling with core rotation. Studies of nitric oxide in particular have shown that $n f(2)$ Rydberg states of NO traverse the Stark manifold to form NO $^+$ in rotational states $N^+ = 2$ and 0 [S3].

Experiments described in the main text operate in a diabatic regime, employing a slew rate of $0.7 \text{ V cm}^{-1} \text{ ns}^{-1}$. Under these conditions, SFI features that appear when the field rises to an amplitude of $F \text{ V cm}^{-1}$ measure electrons bound by energy E_b in cm^{-1} , according to $E_b = 4\sqrt{F}$.

Quasi-free electrons, weakly bound in the attractive potential of more than one cation, ionize at a low field that varies with the number of excess ions in the plasma.

The SFI spectrum presented in the text as Figure 1(c) and shown here as Figure S1 maps the electron binding energy as a function of the initial Rydberg gas density for a molecular nitric oxide ultracold plasma after 500 ns of evolution. At a glance, the spectrum at higher density (10^{12} cm^{-3}) shows direct evidence of either electrons bound to an increasing space charge or a broader distribution of high- n Rydberg states.

This contracts to a narrower distribution of very weakly bound electrons in plasmas of lower density (10^{10} cm^{-3}). Here we observe the spectrum of a residue of molecules with the originally selected principal quantum number of the Rydberg gas, shifted slightly to deeper apparent binding energy by evident l -mixing or slight relaxation in n .

We have used SFI measurements like these to characterize the avalanche and evolution dynamics of a great many Rydberg gases of varying density and initial principal quantum number. Relaxation times vary, but all of these spectra evolve to form the same final spectrum of weakly bound electrons with traces of residual Rydberg gas for systems of low initial density.

III. COUPLED RATE-EQUATION SIMULATIONS OF THE ELECTRON-IMPACT AVALANCHE TO ULTRACOLD PLASMA IN A MOLECULAR RYDBERG GAS

The semi-classical mechanics embodied in a system of coupled rate equations serves well to describe the avalanche of a molecular Rydberg gas to ultracold plasma. In this picture, Rydberg molecule densities,

* Author to whom correspondence should be addressed. Electronic mail: edgrant@chem.ubc.ca

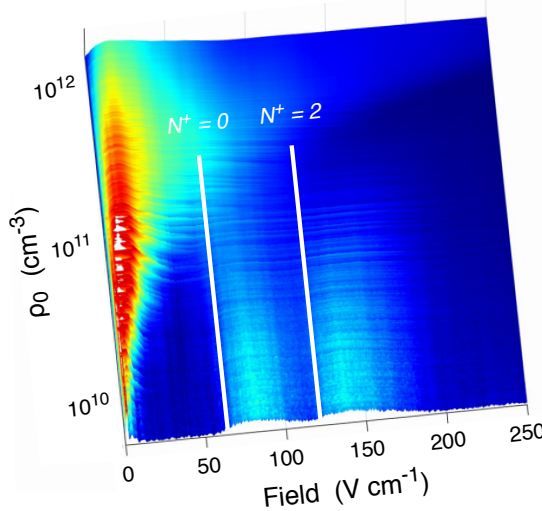


FIG. S1. Selective field ionization spectrum spectrum as a function of initial Rydberg gas density, ρ_0 , after 500 ns of evolution, showing the signal of weakly bound electrons combined with a residual population of 49f(2) Rydberg molecules, (initial principal quantum number, $n_0 = 49$, in the f Rydberg series converging to NO^+ ion rotational state, $N^+ = 2$). After 10 μs , this population sharpens to signal high- n Rydbergs and plasma electrons, with a residue of the initial Rydberg population, shifted slightly to deeper binding energy by l -mixing and perhaps some small relaxation in n . The prominent feature that appears at the lowest values of the ramp field gauges the potential energy of electrons in high Rydberg states bound to single NO^+ ions, combined with electrons bound to the space charge of more than one ion. Notice the binding effect of a slightly greater excess positive charge at the highest initial Rydberg gas densities. The red feature extends approximately to the binding energy of $n_0 = 80$ or 500 GHz.

labeled ρ_i , evolve over a ladder of principal quantum numbers, n_i , according to:

$$-\frac{d\rho_i}{dt} = \sum_j k_{ij}\rho_e\rho_i - \sum_j k_{ji}\rho_e\rho_j + k_{i,ion}\rho_e\rho_i - k_{i,tbr}\rho_e^3 + k_{i,PD}\rho_i \quad (\text{S1})$$

The free-electron density changes as:

$$\frac{d\rho_e}{dt} = \sum_i k_{ion}\rho_e^2 - \sum_i k_{tbr}^i\rho_e^3 - k_{DR}\rho_e^2 \quad (\text{S2})$$

A variational reaction rate formalism determines T_e -dependant rate coefficients, k_{ij} , for electron impact transitions from Rydberg state i to j , k_{ion}^i , for collisional ionization from state i and k_{tbr}^i , for three-body recombination to state i [S4, S5]. Unimolecular rate constants, $k_{i,PD}$, describe the principal quantum number dependant rate of Rydberg predissociation [S6–S8], averaged over azimuthal quantum number, l [S9]. k_{DR} accounts for direct dissociative recombination [S10]

The relaxation of molecules in the manifold of Rydberg states determines the temperature of electrons released by avalanche. Conservation of total energy per unit volume requires:

$$E_{tot} = \frac{3}{2}k_B T_e(t)\rho_e(t) - R \sum_i \frac{\rho_i(t)}{n_i^2} + \frac{3}{2}k_B T \rho_e^{DR} - R \sum_i \frac{\rho_i^{PD}}{n_i^2} \quad (\text{S3})$$

where R is the Rydberg constant for NO, and ρ_e^{DR} and ρ_i^{PD} represent the number of electrons and Rydberg molecules of level i lost to dissociative recombination and predissociation, respectively [S11, S12].

To realistically represent the density distribution produced by crossed-beam laser excitation of the cylindrical distribution of NO ground-state molecules in the molecular beam, we use a concentric system of 100 shells of defined density spanning a Gaussian ellipsoid to 5σ in three dimensions. Avalanche proceeds as determined by the initial Rydberg molecule density of each shell. Each shell conserves the combined density of stationary molecules, ions and neutral fragmentation products. Electrons satisfy local quasi-neutrality, but are otherwise assumed mobile, and thermally equilibrated over the entire volume [S13].

A. The semi-classical evolution of an $n_0 = 80$ Rydberg gas

Figure S2 shows the global evolution of particle densities and electron temperature calculated for an $n_0 = 80$ Rydberg gas at an initial density of $4 \times 10^{10} \text{ cm}^{-3}$ [S13], representing one limit of the SFI spectrum obtained as above for an ultracold plasma in its arrest state after an evolution time of 10 μs . By this point, the real system begins a phase of unchanging composition and very slow expansion that lasts at least a millisecond – as long a period as we can observe it.

The the semi-classical simulation result shown in Figure S2 tells us that the SFI spectrum shown in Figure S1 cannot possibly signal a conventional gas of long lived high-Rydberg molecules. Instead, a proven semi-classical rate model configured for the density distribution of the experiment, predicts the decay of such a high-Rydberg gas to plasma on the timescale of a microsecond or less.

In the model, predissociation consumes residual Rydbergs in all n -levels within a few microseconds and the formation of neutral atomic products quickly slows. This must occur conventionally because the rising electron temperature stabilizes the classical plasma state by suppressing three-body recombination. The real arrested state, however, shows no sign of an electron temperature higher than a few degrees K.

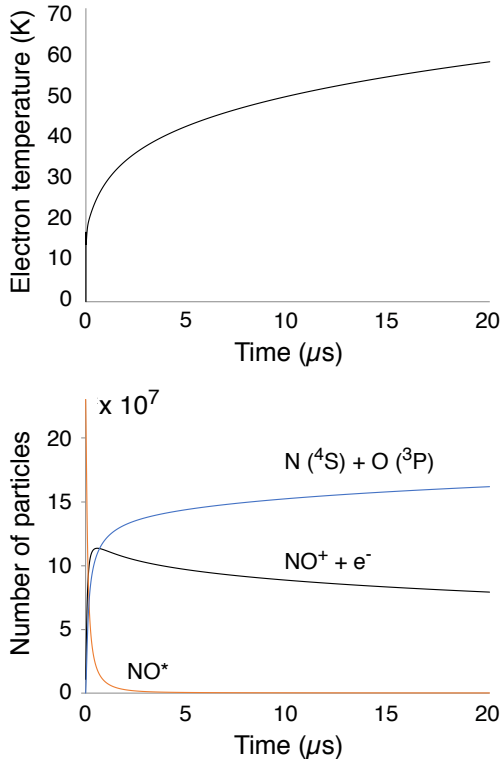


FIG. S2. (lower) Numbers of ions and electrons, Rydberg molecules and neutral dissociation products $N(^4S)$ and $O(^3P)$ as a function of time during the avalanche of an $n_0 = 80$ Rydberg gas of NO to form an ultracold plasma, as predicted by a shell-model coupled rate equation simulation. Here we represent the initial density distribution of the Rydberg gas by a 5σ Gaussian ellipsoid with principal axis dimensions, $\sigma_x = 1.0$ mm, $\sigma_y = 0.55$ mm, $\sigma_z = 0.7$ mm and peak density of 4×10^{10} cm⁻³, as measured for a typical experimental plasma entering the arrest state after an evolution of 10 μ s. The simulation proceeds in 100 concentric shells enclosing set numbers of kinetically coupled particles, linked by a common electron temperature that evolves to conserve energy globally. (upper) Global electron temperature as a function of time.

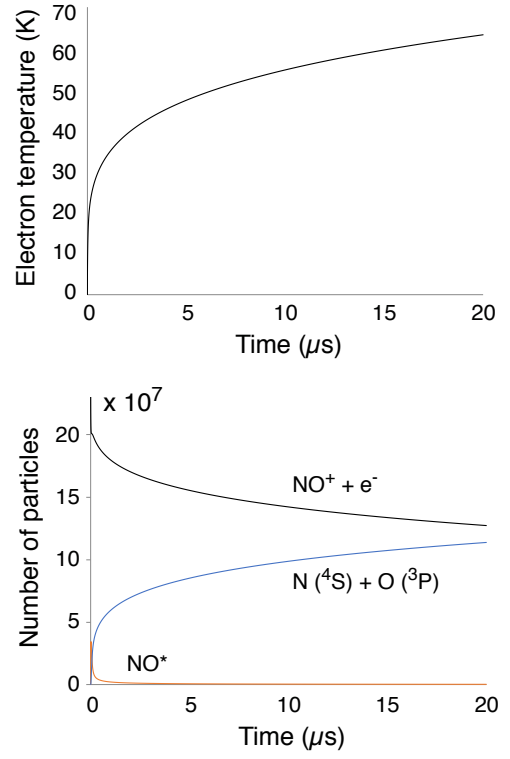


FIG. S3. (lower) Numbers of ions and electrons, Rydberg molecules and neutral dissociation products $N(^4S)$ and $O(^3P)$ as a function of time during the evolution of an ultracold plasma of NO^+ ions and electrons, as predicted by a shell-model coupled rate equation simulation. Here we represent the initial density distribution of the plasma by a 5σ Gaussian ellipsoid with principal axis dimensions, $\sigma_x = 1.0$ mm, $\sigma_y = 0.55$ mm, $\sigma_z = 0.7$ mm, peak density of 4×10^{10} cm⁻³ and initial electron temperature, $T_e(0) = 5$ K, as measured for a typical experimental plasma entering the arrest state after an evolution of 10 μ s. The simulation proceeds in 100 concentric shells enclosing set numbers of kinetically coupled particles, linked by a common electron temperature that evolves to conserve energy globally. (upper) Global electron temperature as a function of time.

B. The semi-classical evolution of a fully ionized ultracold plasma with $T_e(0) = 5$ K

Let us instead test instead the kinetic stability of a conventional ultracold plasma composed entirely of ions and electrons. Again, we assume initial conditions that fit with the observed properties of the arrest state: NO^+ and electrons present at a density of 4×10^{10} cm⁻³ in an ellipsoid with Gaussian dimensions, $\sigma_x = 1.0$ mm, $\sigma_y = 0.55$ mm, $\sigma_z = 0.7$ mm, represented by simulations evolving in 100 shells, with electron temperature equilibration [S13]. In keeping with the very slow rate of plasma expansion observed in the experiment, we set the initial electron temperature to 5 K.

Figure S3 shows how this classical arrest state evolves in time. The formation and rapid decay of NO Rydberg

molecules signifies an immediate process of three-body recombination, which decreases the charged particle density of the plasma. Predissociation reduces the steady-state density of Rydberg molecules to a value of nearly zero, but three-body recombination persists as shown by the rising density of neutral atom fragments. Eventually, this process slows as the electron temperature rises. Could this hot-electron ultracold plasma represent the end state of arrested relaxation? Absolutely not. As detailed in the next section, a plasma with an electron temperature of 60 K would expand to a volume larger than our experimental chamber in less than 100 μ s.

IV. AMBIPOLEAR EXPANSION IN A PLASMA WITH AN ELLIPSOIDAL DENSITY DISTRIBUTION

The self-similar expansion of a spherical Gaussian plasma is well-described by an analytic solution of the Vlasov equations for electrons and ions with self-consistent electric fields. For a distribution of width σ , in the limit of $T_e \gg T_i$, this solution reduces to [S14]:

$$e\nabla\phi = k_B T_e \rho^{-1} \nabla\rho = -k_B T_e \frac{r}{\sigma^2} \quad (\text{S4})$$

In essence, the thermal pressure of the electron gas produces an electrostatic force that radially accelerates the ion density distribution according to the gradient in the electrostatic potential. In approximate terms, the expanding electrons transfer kinetic energy to the ions, accelerating the distribution to an average ballistic velocity,

$$k_B T_e \approx m_i \langle v_i^2 \rangle \quad (\text{S5})$$

The velocity varies linearly with radial distance, $\partial_t r = \gamma r$, where γ falls with time as the distribution expands, and the electron temperature cools according to $\partial_t T_e = -2\gamma T_e$.

To model the ellipsoidal plasma, we represent its charge distribution by a set of concentric shells. In this shell model, the density difference from each shell j to shell $j+1$ establishes a potential gradient that determines the local electrostatic force in each principal axis direction, k [S15]:

$$\begin{aligned} \frac{e}{m_i} \nabla\phi_{k,j}(t) &= \frac{\partial u_{k,j}(t)}{\partial t} \\ &= \frac{k_B T_e(t)}{m_i \rho_j(t)} \frac{\rho_j(t) - \rho_{j+1}(t)}{r_{k,j}(t) - r_{k,j+1}(t)} \end{aligned} \quad (\text{S6})$$

where $\rho_j(t)$ represents the density of ions in shell j .

The radial coordinates of each shell evolve according to its instantaneous velocity along each axis, $u_{k,j}(t)$.

$$\frac{\partial r_{k,j}(t)}{\partial t} = u_{k,j}(t) = \gamma_{k,j}(t) r_{k,j}(t) \quad (\text{S7})$$

which in turn determines shell volume and thus its density, $\rho_j(t)$. The electron temperature supplies the thermal energy that drives this ambipolar expansion. Ions accelerate and T_e falls according to:

$$\frac{3k_B}{2} \frac{\partial T_e(t)}{\partial t} = -\sum_j N_j \sum_{k,j} N_j u_{k,j}(t) \frac{\partial u_{k,j}(t)}{\partial t} \quad (\text{S8})$$

Figure S4 compares the ambipolar expansion of an ellipsoidal plasma, simulated for an initial volume with the starting dimensions described above and an initial electron temperature of 60 K, compared with the time evolution of the Gaussian width measured in z by experiment. Note that the choice of a large initial

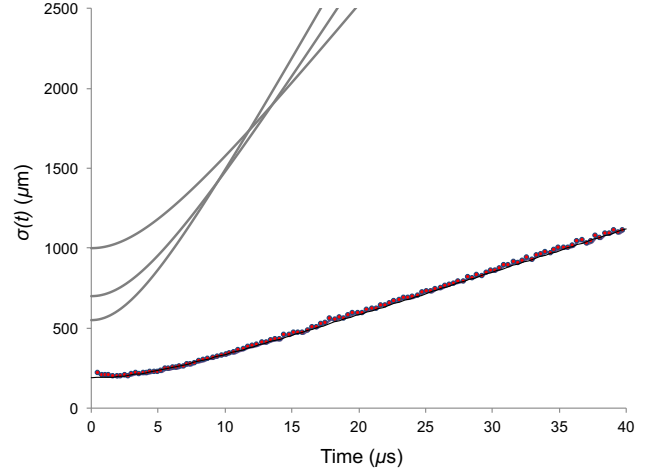


FIG. S4. Hydrodynamic expansion of a Gaussian ellipsoid with the dimensions measured at 10 μs for the typical arrested plasma described above, modeled by a 100-shell simulation, assuming an electron temperature that rises to 60 K, with curves, reading from the bottom on the left, for $\sigma_y(t)$, $\sigma_z(t)$ and $\sigma_x(t)$. The lower curve with data shows the measured expansion of a typical molecular NO ultracold plasma with a Vlasov fit for $T_e = 3$ K.

volume intrinsically slows the simulated expansion. Yet, nevertheless, the electron heating that arises inevitably from three-body recombination in a classical ultracold plasma demands a rate of expansion that is completely unsupported by experimental observation.

V. EFFECTIVE MANY-BODY HAMILTONIAN

Experimental observations tell us that the molecular ultracold plasma of nitric oxide evolves to a state of arrested relaxation in which extravalent electrons occupy a narrow distribution of weakly bound states. This distribution of states supports a vast distribution of pair-wise interactions, creating a random potential landscape. Resonant dipole-dipole interactions in this dense manifold of basis states cause excitation exchange. In the disorder potential, these processes are dominated by low energy-excitations involving L states in number, where we expect L to be small (from 2 to 4). The most probable interactions select L -level systems composed of different basis states from dipole to dipole. Thus, the states $|e^1\rangle$, $|e^2\rangle$... $|e^L\rangle$ vary from one dipole to the next and from time to time.

Representing excitations by spins, we can write an XY model [S16] that describes these interactions in terms of their effective spin dynamics

$$H_{\text{eff}} = \sum_i \epsilon_i \hat{S}_i^z + \sum_{i,j} J_{ij} (\hat{S}_i^+ \hat{S}_j^- + h.c.) \quad (\text{S9})$$

where \hat{S} in each case denotes a spin- L operator defined as $\hat{S}^\gamma = \hbar \hat{o}^\gamma / 2$, for which σ^γ is the corresponding spin- L

Pauli matrix that spans the space of the L active levels and $\gamma = x, y$ or z . *h.c.* refers to Hermitian conjugate.

Let us now consider specific examples of this construction.

A. $L = 2$ case

Figure S5 diagrams a case that is uniquely defined for every pair of interacting dipoles. In the limit of isolated pairs, this two-level interaction is exactly resonant. Conditions described below randomly displace these energy level positions.

For each particular dipole i , described by states $|e_i^1\rangle$ and $|e_i^2\rangle$, let us define a projection operator for the higher-energy state (which we will call spin-up) $\hat{\sigma}_i^{e^2} = |e_i^2\rangle\langle e_i^2| = (1 + \hat{\sigma}_i^z)/2$ and the lower-energy state (spin-down) $\hat{\sigma}_i^{e^1} = |e_i^1\rangle\langle e_i^1| = (1 - \hat{\sigma}_i^z)/2$. Thus, we can represent the two levels of a dipole i , with an energy spacing ϵ_i , by a one-body operator $\epsilon_i \hat{S}_i^z = (\hbar\epsilon_i/2)\hat{\sigma}_i^z$. This defines an energy $\pm\hbar\epsilon_i/2$ depending on which state $|e_i^2\rangle$ or $|e_i^1\rangle$ is occupied, respectively, *i.e.* $|e_i^2\rangle \equiv |\uparrow_i\rangle$ and $|e_i^1\rangle \equiv |\downarrow_i\rangle$.

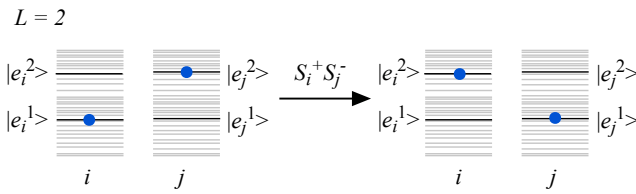


FIG. S5. Schematic diagram representing two Rydberg molecules, i and j , dipole coupled in the two-level approximation. In every case, the disorder in the environment of each molecule perturbs the exact energy level positions of $|e_i\rangle$ and $|e_j\rangle$.

The onsite energy is given by $\epsilon_i = E_i^{12} + D_i$ [S17], where E_i^{12} is the energy separation between the two states $|e_i^1\rangle$ and $|e_i^2\rangle$ evaluated for the local Hamiltonian h_i . h_i varies with the random potential landscape from one dipole to the next and thus is responsible for the diagonal disorder in the onsite term. $D_i = \sum_{j \neq i} \langle e_i^2, e_j^1 | V_{i,j}^{dd} | e_i^2, e_j^1 \rangle - \langle e_i^1, e_j^1 | V_{i,j}^{dd} | e_i^1, e_j^1 \rangle$ represents the shift in a dipole's energy due to dipole-dipole interactions [S17]. This term is identically zero for parity-conserving states [S18].

Lowering and raising operators, $\hat{\sigma}_i^- = |e_i^1\rangle\langle e_i^2|$ and its Hermitian conjugate $\hat{\sigma}_i^+ = |e_i^2\rangle\langle e_i^1|$, define a resonant spin flip-flop between dipoles i and j : $J_{ij}(\hat{S}_i^+ \hat{S}_j^- + h.c.) = (\hbar J_{ij}/2)(\hat{\sigma}_i^+ \hat{\sigma}_j^- + h.c.)$ with amplitude $J_{ij} = t_{ij}/r_{ij}^3$; $t_{ij} = \langle e_i^2, e_j^1 | V_{i,j}^{dd} | e_i^1, e_j^2 \rangle$. This refers to the dipole-dipole mediated transfer of excitation [S17] represented by, for

example, $\hat{S}_i^+ \hat{S}_j^- |\downarrow_i\rangle |\uparrow_j\rangle = |\uparrow_i\rangle |\downarrow_j\rangle$ *i.e.* $|e_i^2\rangle |e_j^1\rangle \xrightarrow{\hat{S}_i^+ \hat{S}_j^-} |e_i^1\rangle |e_j^2\rangle$. We can expect this class of matrix element to be non-zero for many of the local eigenstates of h_i and h_j ,

as the dipole-dipole operator couples states of different parity, limited only by a few selection rules [S18].

Additionally, we note that dipole-dipole interactions lead to a two-body Ising term of the form $\hat{S}_i^z \hat{S}_j^z$. This term originates from dipole-dipole induced shifts of pairs of dipoles [S17] and has an amplitude $\langle e_i^2, e_j^2 | V_{i,j}^{dd} | e_i^2, e_j^2 \rangle + \langle e_i^1, e_j^1 | V_{i,j}^{dd} | e_i^1, e_j^1 \rangle$. This term is also identically zero for parity conserving states [S18]. Since, the arrested phase includes no external parity-breaking fields and neglecting local field fluctuations, we assume $D_i = 0 \rightarrow \epsilon_i = E_i^{12}$ and no dipole-dipole induced Ising interaction.

B. $L > 2$ cases

We can easily imagine systematic coupling schemes that involve three or four L -level interactions. Excitation transfer still governs the dynamics via terms like $J_{ij}(\hat{S}_i^+ \hat{S}_j^- + h.c.)$, where the \hat{S} operators live in the active L -dimensional subspaces. Figures S6 and S7 schematically detail examples of these interactions.

$L = 3$

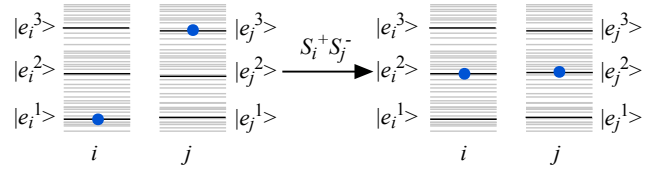


FIG. S6. Schematic diagram representing two Rydberg molecules, i and j , dipole coupled in the limits of $L = 3$. In the very high state density of the quenched ultracold plasma, the displacement of $|e_i^2\rangle$ and $|e_j^2\rangle$ will lessen the significance of $L = 3$ interactions compared with the case of $L = 4$.

Figure S6 represents an interaction of overwhelming importance in studies of Rydberg quantum optics. Typically, a narrow bandwidth laser excites a resonant pair state, such as $23P_{3/2} + 23P_{3/2} \leftrightarrow 23s + 24s$ in Cs [S19]. Excitation transfer in this $L = 3$ case operates for example as:

$$\hat{S}_i^+ \hat{S}_j^- |S_i = -1\rangle |S_j = 1\rangle = |S_i = 0\rangle |S_j = 0\rangle, \quad (S10)$$

$$\text{i.e. } |e_i^1\rangle |e_j^3\rangle \xrightarrow{\hat{S}_i^+ \hat{S}_j^-} |e_i^2\rangle |e_j^2\rangle$$

For a gas of Rydberg molecules occupying a dense manifold of disordered states, the case of $L = 3$ becomes an operationally indistinguishable special case of the more general $L = 4$ interaction, which maps onto a spin of $3/2$.

Here, we represent the interaction as an excitation transfer that operates as:

$$\begin{aligned} \hat{S}_i^+ \hat{S}_j^- |S_i = -3/2\rangle |S_j = 3/2\rangle \\ = |S_i = -1/2\rangle |S_j = 1/2\rangle, \end{aligned} \quad (S11)$$

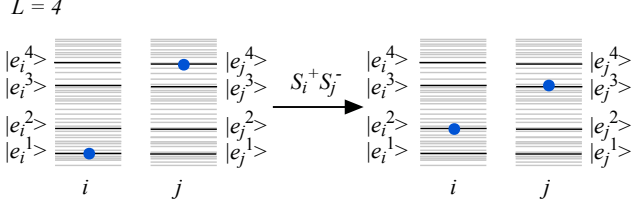


FIG. S7. Schematic diagram representing two Rydberg molecules, i and j , dipole coupled in the limits of $L = 4$. The high state density and strong disorder in the quenched ultracold plasma gives this case of $L = 4$ greater significance than the restrictive limit of $L = 3$

$$\text{i.e. } |e_i^1\rangle |e_j^4\rangle \xrightarrow{\hat{S}_i^+ \hat{S}_j^-} |e_i^2\rangle |e_j^3\rangle.$$

We can extend such sequences to higher L , but low-energy resonant dipole-dipole excitation exchange in the dense manifold of basis states will most prominently involve a small number of L -levels per dipole.

VI. INDUCED VAN DER WAALS INTERACTIONS

For $|J_{ij}| \ll W$, sequences of interactions add Ising terms that describe a van der Waals shifts of pairs of dipoles [S20]. Consider, for example, three mutually nearest-neighbour spins i , j and k in the $L = 2$ case. A third-order process couples spins i and j via spin k in the following fashion: $|\downarrow_i, \uparrow_j, \uparrow_k\rangle \xrightarrow{\hat{S}_i^+ \hat{S}_j^-} |\uparrow_i, \downarrow_j, \uparrow_k\rangle \xrightarrow{\hat{S}_j^+ \hat{S}_k^-} |\uparrow_i, \uparrow_j, \downarrow_k\rangle \xrightarrow{\hat{S}_k^+ \hat{S}_i^-} |\downarrow_i, \uparrow_j, \uparrow_k\rangle$; defining a self interaction that changes the pairwise energies of i , j .

U_{ij} is inherently random owing to the randomness in J_{ij} . It is also important to note that this limit gives rise to additional perturbative processes that renormalize the local onsite fields by van der Waals terms and slightly affect the pairwise flip-flop amplitudes [S20–S22]. We simply absorb these effects in the definitions of ϵ_i and J_{ij} .

Taken together with Eq (S9) this result yields a general spin model with dipole-dipole and van der Waals interactions:

$$\begin{aligned} H_{\text{eff}} = & \sum_i \epsilon_i \hat{S}_i^z + \sum_{i,j} J_{ij} (\hat{S}_i^+ \hat{S}_j^- + h.c.) \\ & + \sum_{i,j} U_{ij} \hat{S}_i^z \hat{S}_j^z \end{aligned} \quad (\text{S12})$$

where $U_{ij} = D_{ij}/r_{ij}^6$ and $D_{ij} = t_{ij}^2 \tilde{J}/W^2$.

The appearance of this third term underlines the many-body nature of Eq (S9). Even in this extreme limit, its dynamics are non-trivial, clearly involving more than spin flip-flops with emergent correlations between spins.

Non-resonant spin-spin interactions — The appearance of the term, $\sum_{i,j} U_{ij} \hat{S}_i^z \hat{S}_j^z$, underlines

the many-body nature of this model. One obtains this term by treating J_{ij} as a perturbation in Eq (S9) [S20]. For the $L = 2$ case, this occurs at the third order, while for all other L , this term appears at the second order [S20]. Thus, such a term arises generally in the $|J_{ij}| \ll W$ limit in three dimensions.

The van der Waals interactions occur with an amplitude, $U_{ij} \approx J_{ij}^2 \tilde{J}/W^2$, where \tilde{J} estimates J_{ij} at the average distance separating spins. We do not expect these interactions to depend strongly on the off-diagonal disorder, as they arise from the off-resonant part of $\sum_{i,j} J_{ij} (\hat{S}_i^+ \hat{S}_j^- + h.c.)$, which presumably does not cause real transitions [S20]. Thus, we can rationalize the use of \tilde{J} here as an average weighting term. We leave the task of studying the effect of off-diagonal disorder to future work.

Non-resonant onsite interactions — It is also important to note that this limit gives rise to additional perturbative processes that renormalize the local onsite fields $\sum_i \epsilon_i \hat{S}_i^z$ by van der Waals terms [S20].

Similar considerations from a completely different atomistic perspective verify that this term is approximately $\sum_{l \neq i} h C_6^{ij} / r_{ij}^6$ where h is the Planck constant and C_6^{ij} denotes the C_6 coefficients for the van der Waals interaction between the off-resonant dipoles i and j [S21, S22].

The induced onsite terms will also vary randomly owing to the randomness in the potential landscape. We simply absorb such terms in the definition of ϵ_i .

VII. RESONANCE COUNTING AND THE NUMBER OF DIPOLES IN THE QUENCHED ULTRACOLD PLASMA

Ref [S20] considers the problem of delocalization via resonance counting arguments in the model of Eq S12 for the general case of $\alpha < \beta$, under conditions for which $d > d_c$. Here α refers to the power law that regulates J_{ij} and β refers to U_{ij} . d and d_c stand for dimensionality and critical dimensionality. This work concludes that delocalization occurs at arbitrary disorder given sufficient system size.

For local disorder, W , and average spin flip-flop amplitude, \tilde{J} , the resonant pair criterion defines, N_c , a critical number of dipoles above which the system delocalizes. Here, we compare this theoretical estimate with an accurate experimental measure of the number of dipoles present in the arrest state of the quenched ultracold plasma.

Controlled conditions of supersonic expansion precisely define the cylindrical density distribution of nitric oxide in the molecular beam [S1]. Co-propagating laser beams, Gaussian ω_1 and ω_2 , cross orthogonally in the x, y plane to define a Gaussian ellipsoidal excitation volume.

When ω_2 saturates the second step of double resonance, the intensity of ω_1 controls the peak density of the Rydberg gas volume up to a maximum of $6 \times$

10^{12} cm $^{-3}$, obtained upon saturation of the first step. Density varies from shot to shot, and we have developed an accurate means of classifying and binning individual SIF traces according to initial Rydberg gas peak density, as displayed in Figure S1. Coupled rate simulations describing the kinetics of the avalanche of Rydberg gas to plasma confirm these estimates of peak density.

TABLE S1. Distribution of ions in an idealized Gaussian ellipsoid shell model of a quenched ultracold plasma of NO as it enters the arrest state with a peak density of 4×10^{10} cm $^{-3}$, $\sigma_x = 1.0$ mm, $\sigma_y = 0.55$ mm and $\sigma_z = 0.70$ mm. At this point, the quasi-neutral plasma contains a total of 1.9×10^8 NO $^+$ ions (NO Rydberg molecules). Its average density is 1.4×10^{10} cm $^{-3}$ and the mean distance between ions is 3.32 μm .

Shell Num	Density cm $^{-3}$	Volume cm 3	Particle Number	Fraction $\times 100$	a_{ws} μm
1	4.0×10^{10}	1.8×10^{-6}	7.0×10^4	0.04	1.81
2	3.9×10^{10}	1.1×10^{-5}	4.4×10^5	0.23	1.83
3	3.7×10^{10}	9.0×10^{-5}	3.3×10^6	1.75	1.86
4	3.3×10^{10}	2.8×10^{-4}	9.3×10^6	4.87	1.93
5	2.6×10^{10}	8.3×10^{-4}	2.2×10^7	11.52	2.08
6	2.1×10^{10}	1.2×10^{-3}	2.6×10^7	13.40	2.26
7	1.5×10^{10}	1.8×10^{-3}	2.8×10^7	14.46	2.49
8	1.1×10^{10}	2.4×10^{-3}	2.6×10^7	13.81	2.78
9	7.4×10^9	3.4×10^{-3}	2.5×10^7	13.28	3.19
10	4.3×10^9	5.1×10^{-3}	2.2×10^7	11.56	3.81
11	2.0×10^9	8.3×10^{-3}	1.7×10^7	8.85	4.89
12	5.6×10^8	1.7×10^{-2}	9.4×10^6	4.94	7.51
13	7.9×10^7	3.1×10^{-2}	2.4×10^6	1.27	14.47
14	4.0×10^6	5.6×10^{-2}	2.3×10^5	0.12	38.96
15	4.4×10^4	1.0×10^{-1}	4.6×10^3	0.00	176.22

Two methods of plasma tomography determine the evolution of plasma size and relative density distribution as a function of time. In the SFI apparatus, a perpendicular imaging grid that translates in the molecular beam propagation direction, z , yields an electron signal waveform that gauges the changing plasma density and width as a function of evolution time. This waveform, followed to a point of evident arrest at about 5 μs , and well beyond, as illustrated by Figure 1 in the main text, establish a case for arrested relaxation.

Images projected in the x, y plane together with waveforms in z , recorded after nearly 0.5 ms of flight, detail a slow ballistic expansion in Cartesian coordinates that we extrapolate back to an evolution time of 10 μs to determine the absolute density distribution of the arrested ultracold plasma, described by the shell model presented in Table S1. This representation neglects the redistribution of charge density associated with the initial stages of bifurcation. The total number of ions represented by this distribution remains constant for as long as we can measure it in our long flight-path instrument, at least a half millisecond.

The ion density averaged over shells determines $\langle |\mathbf{r}_{ij}| \rangle$. This average distance between dipoles, combined with a rough upper-limiting estimate of the average dipole-

dipole matrix element, $\langle t_{ij} \rangle$, based on values computed for a $\Delta n = 0$ Föster resonant interaction in Li [S22], yields an upper-limiting estimate of \tilde{J} .

However, interaction with charged particles in the plasma environment perturbs the electronic structure of individual Rydberg molecules. This diminishes the probability of finding resonant target states, decreasing the real value of \tilde{J} , and giving rise to a rarity and randomness of resonant dipole-dipole interactions distributed over a huge state space defined by the measured distribution of electron binding energies, W .

As noted in Figure S1, a simple measure of the width of the plasma feature in the delayed SFI spectrum determines W . Table S2 summarizes this and other parameters of the arrest state derived from experiment, including the \tilde{J} for Li under our conditions as an upper limit.

For short range interactions in a one-dimensional spin chain, perturbative arguments applied to disordered interacting spin models, such as the one above, predict many-body localization [S23]. However, in higher dimensions especially, long-range resonant interactions play an important role in defining the conditions under which localization can occur. It is generally accepted that interactions governed by a coupling amplitude, J_{ij} that decreases with distance as $1/r_{ij}^\beta$ delocalizes any system at finite temperature for which the dimension, d exceeds $\beta/2$.

However, building on ideas introduced by Anderson [S24] and Levitov [S25], Burin [S20] offers a means by which to test a dimensionally constrained system for conditions that favor the onset of delocalization. He uses a perturbation approach that defines limits over which localization can occur in a system as modeled above in which delocalization proceeds by the Ising interaction of extended resonant pairs.

In this picture, a system that violates the dimension constraint delocalizes for an arbitrary size of disorder whenever the number of dipoles exceeds a critical number, N_c , which is determined by the disorder width, W and the average coupling strength, \tilde{J} . Coupling terms in the Hamiltonian defined by Eq S12 scale in r according to $\alpha = 3$, $\beta = 6$ and $d = 3$. This sets a critical number of dipoles defined by the quantity, $N_c = (W/\tilde{J})^4$ [S20]. For the arrest state defined by the density distribution described by the elliptical shell model in Table S1, the measured W taken with our upper limiting estimate for \tilde{J} , yields $N_c = 3.6 \times 10^9$.

Considering this value of N_c in relation to the average density of the system at arrest defines R^* , an effective distance between resonant dipoles at which point this occurs [S20]. For the conditions described in Table S1, this coupling would occur in a system large enough to contain 3.6×10^9 dipoles a distance of 4 mm or more. At this distance, our upper-limiting dipole-dipole matrix element would predict a characteristic irreversible transition time, τ^* on the order of one second [S26].

TABLE S2. Resonance counting parameters in the arrest state of the quenched ultracold plasma. The disorder width W , taken directly from the width of the plasma feature in the SIF spectrum, combined with \tilde{J} – derived from a rough upper-limiting estimate of the average dipole-dipole matrix element, $\langle t_{ij} \rangle$, based on values computed for $\Delta n = 0$ interactions in alkali metals [S22], together with the mean distance between NO^+ ions in the shell model ellipsoid – determines N_c . a critical number of dipoles required for delocalization. R^* describes the length scale for delocalization and τ^* denotes the delocalization time, given a sufficient number of dipoles at the average density of the experiment. Note that the ultracold plasma quenched experimentally contains an order of magnitude fewer than N_c dipoles.

W GHz	$\langle t_{ij} \rangle$ GHz(μm) ³	$\langle \mathbf{r}_{ij} \rangle$ μm	\tilde{J} GHz	N_c	R^* μm	τ^* s
500	75	3.3	2.0	3.6×10^9	4000	0.85

We note that the quenched ultracold plasma formed experimentally relaxes to a volume that contains an order of magnitude fewer dipoles than N_c , as determined for this case by the model of Ref [S20].

As we attempt to convey above, the experiment yields plasmas of well defined density distribution and total number of dipoles. However, the precise nature of the associated quantum states and their dipole-dipole interaction is much less well known. This limits the certainty with which we can determine N_c . What's more perturbation theory in a locator expansion formulation may not accurately define the limiting conditions for MBL in higher dimensions [S27].

Rare thermal regions (Griffiths regions) are thought to destabilize MBL systems of higher dimension [S28–S32], creating a glassy state, characterized by a slow

evolution to a delocalized phase. However, other results contradict this notion, and support the possibility of localization in all dimensions [S33]. An added feature in the self-assembly of the molecular ultracold plasma may preclude destabilization by rare thermal regions: Should the quenched plasma develop a Griffiths region as a site for delocalization to occur, the predissociation of relaxing NO molecules would promptly deplete that region to a void of no consequence.

In any event, the quenched plasma seems consistently able to find the conditions necessary for arrested relaxation. A great many different avalanche starting conditions, defined by varying initial Rydberg gas density and initial principal quantum number, all evolve to retain comparable internal energy and yield an arrest state with much the same density distribution as that described by the shell model detailed in Table S1.

ACKNOWLEDGMENTS

This work was supported by the US Air Force Office of Scientific Research (Grant No. FA9550-12-1-0239), together with the Natural Sciences and Engineering Research Council of Canada (NSERC), the Canada Foundation for Innovation (CFI), the British Columbia Knowledge Development Fund (BCKDF) and the Stewart Blusson Quantum Matter Institute (SBQMI). JS gratefully acknowledges support from the Harvard-Smithsonian Institute for Theoretical Atomic, Molecular and Optical Physics (ITAMP). We have benefited from helpful interactions with Rahul Nandkishore, Shivaji Sondhi and Alexander Burin. We also gratefully acknowledge discussions with Rafael Hanel, James Keller, Rodrigo Vargas, Arthur Christianen, Markus Schulz-Weiling, Hossein Sadeghi and Luke Melo.

-
- [S1] M Schulz-Weiling, H Sadeghi, J Hung, and E R Grant, “On the evolution of the phase-space distributions of a non-spherical molecular ultracold plasma in supersonic beam,” *J Phys B* **49**, 193001 (2016).
- [S2] T F Gallagher, *Rydberg Atoms* (Cambridge University Press, 2005).
- [S3] R Patel, N Jones, and H Fielding, “Rotational-state-selective field ionization of molecular Rydberg states,” *Phys Rev A* **76**, 043413 (2007).
- [S4] P. Mansbach and J. Keck, “Monte carlo trajectory calculations of atomic excitation and ionization by thermal electrons,” *Phys. Rev.* **181**, 275–289 (1969).
- [S5] T Pohl, D Vrinceanu, and H R Sadeghpour, “Rydberg atom formation in ultracold plasmas: Small energy transfer with large consequences,” *Phys. Rev. Lett.* **100**, 223201 (2008).
- [S6] M Bixon and J Jortner, “Intramolecular coupling between non-penetrating high molecular Rydberg states,” *Molecular Physics* **89**, 373–401 (1996).
- [S7] E Murgu, J D D Martin, and T F Gallagher, “Stabilization of predissociating nitric oxide Rydberg molecules using microwave and radio-frequency fields,” *J. Chem. Phys.* **115**, 7032 (2001).
- [S8] F Remacle and M Vrakking, “Decay Dynamics of the Predissociating High Rydberg States of NO,” *J Phys Chem A* **102**, 9507–9517 (1998).
- [S9] W A Chupka, “Factors affecting lifetimes and resolution of Rydberg states observed in zero-electron-kinetic-energy spectroscopy,” *J Chem Phys* **98**, 4520–4530 (1993).
- [S10] I F Schneider, I Rabadán, L Carata, L Andersen, A Suzor-Weiner, and J Tennyson, “Dissociative recombination of NO: calculations and comparison with experiment,” *J Phys B* **33**, 4849–4861 (2000).
- [S11] N. Saquet, J. P. Morrison, M. Schulz-Weiling, H. Sadeghi, J. Yiu, C. J. Rennick, and E. R. Grant, “On the formation and decay of a molecular ultracold plasma,” *J Phys B* **44**, 184015 (2011).
- [S12] N Saquet, J P Morrison, and E R Grant, “Recombinative dissociation and the evolution of a molecular ultracold plasma,” *J Phys B* **45**, 175302 (2012).

- [S13] R Haenel, M Schulz-Weiling, J Sous, H Sadeghi, M Aghigh, L Melo, J S Keller, and E R Grant, “Arrested relaxation in an isolated molecular ultracold plasma,” Phys Rev A **96**, 023613 (2017).
- [S14] D S Dorozhina and V E Semenov, “Exact Solution of Vlasov Equations for Quasineutral Expansion of Plasma Bunch into Vacuum,” Phys. Rev. Lett. **81**, 2691–2694 (1998).
- [S15] H Sadeghi and E R Grant, “Dissociative recombination slows the expansion of a molecular ultracold plasma,” Phys Rev A **86**, 052701 (2012).
- [S16] S Sachdev, *Quantum phase transitions* (Wiley Online Library, 2007).
- [S17] V M Agranovich, *Excitations in organic solids*, Vol. 142 (Oxford: Oxford University Press, 2009).
- [S18] J M Brown and A Carrington, *Rotational spectroscopy of diatomic molecules* (Cambridge University Press, 2003).
- [S19] J H Gurian, P Cheinet, P Huillery, A Fioretti, J Zhao, P L Gould, D Comparat, and P Pillet, “Observation of a Resonant Four-Body Interaction in Cold Cesium Rydberg Atoms,” Phys Rev Lett **108**, 023005 (2012).
- [S20] A L Burin, “Localization in a random XY model with long-range interactions: Intermediate case between single-particle and many-body problems,” Phys. Rev. B **92**, 104428 (2015).
- [S21] H. Zoubi, A. Eisfeld, and S. Wüster, “Van der Waals-stabilized Rydberg aggregates,” Phys. Rev. A **89**, 053426 (2014).
- [S22] H Zoubi, “Van der Waals interactions among alkali Rydberg atoms with excitonic states,” J. Phys. B **48**, 185002 (2015).
- [S23] J Z Imbrie, “Diagonalization and many-body localization for a disordered quantum spin chain,” Physical Review Letters **117**, 027201 (2016).
- [S24] P W Anderson, “Absence of diffusion in certain random lattices,” Phys. Rev. **109**, 1492–1505 (1958).
- [S25] L S Levitov, “Critical hamiltonians with long range hopping,” Ann. Phys. **8**, 697–706 (1999).
- [S26] A L Burin, “Energy delocalization in strongly disordered systems induced by the long-range many-body interaction,” arXiv preprint cond-mat/0611387 (2006).
- [S27] R M Nandkishore and S L Sondhi, “Many body localization with long range interactions,” Phys Rev X **7**, 041021 (2017).
- [S28] S Gopalakrishnan, M Müller, V Khemani, M Knap, E Demler, and D A Huse, “Low-frequency conductivity in many-body localized systems,” Phys. Rev. B **92**, 104202 (2015).
- [S29] S Gopalakrishnan, K Agarwal, E A Demler, D A Huse, and M Knap, “Griffiths effects and slow dynamics in nearly many-body localized systems,” Phys. Rev. B **93**, 134206 (2016).
- [S30] W De Roeck and F Huveneers, “Stability and instability towards delocalization in many-body localization systems,” Phys. Rev. B **95**, 155129 (2017).
- [S31] K Agarwal, E Altman, E Demler, S Gopalakrishnan, D A Huse, and M Knap, “Rare-region effects and dynamics near the many-body localization transition,” Ann. Phys. (Amsterdam) **529**, 1600326 (2017).
- [S32] P Ponte, C R Laumann, D A Huse, and A Chandran, “Thermal inclusions: how one spin can destroy a many-body localized phase.” Phil. Trans. R. Soc. A **375**, 20160428 (2017).
- [S33] A. Chandran, A. Pal, C. R. Laumann, and A. Scardicchio, “Many-body localization beyond eigenstates in all dimensions,” Phys. Rev. B **94**, 144203 (2016).